Criteria voor goed rechtswetenschappelijk onderzoek. De omgekeerde route

Smith, C.E.; Geelhoed, W.; Dubelaar, M.J.; Haar, B.P. ter; Rijn van Alkemade, J. van; Willigenburg, K. van; ... ; Deijl, E. v.d.

Citation
Smith, C. E., Geelhoed, W., Dubelaar, M. J., Haar, B. P. ter, Rijn van Alkemade, J. van, Willigenburg, K. van, … Deijl, E. v.d. (2008). Criteria voor goed rechtswetenschappelijk onderzoek. De omgekeerde route. *Monthly Notices Of The Royal Astronomical Society, 83*(12), 685-690. Retrieved from https://hdl.handle.net/1887/49325

Version:	Not Applicable (or Unknown)
License:	Leiden University Non-exclusive license
Downloaded from:	https://hdl.handle.net/1887/49325

Note: To cite this publication please use the final published version (if applicable).

Monthly Notices
of the
ROYAL ASTRONOMICAL SOCIETY

MNRAS **450,** 2291–2305 (2015) doi:10.1093/mnras/stv746

Lunar occultation of the diffuse radio sky: LOFAR measurements between 35 and 80 MHz

H. K. Vedantham,[1⋆] L. V. E. Koopmans,[1] A. G. de Bruyn,[1,2] S. J. Wijnholds,[2] M. Brentjens,[2] F. B. Abdalla,[3] K. M. B. Asad,[1] G. Bernardi,[4,5,6] S. Bus,[1] E. Chapman,[3] B. Ciardi,[7] S. Daiboo,[1] E. R. Fernandez,[1] A. Ghosh,[1] G. Harker,[3] V. Jelic,[1] H. Jensen,[8] S. Kazemi,[1] P. Lambropoulos,[1] O. Martinez-Rubi,[1] G. Mellema,[8] M. Mevius,[1] A. R. Offringa,[9] V. N. Pandey,[1] A. H. Patil,[1] R. M. Thomas,[1] V. Veligatla,[1] S. Yatawatta,[2] S. Zaroubi,[1] J. Anderson,[10,11] A. Asgekar,[2,12] M. E. Bell,[13] M. J. Bentum,[2,14] P. Best,[15] A. Bonafede,[16] F. Breitling,[11] J. Broderick,[17] M. Brüggen,[16] H. R. Butcher,[9] A. Corstanje,[18] F. de Gasperin,[16] E. de Geus,[2,19] A. Deller,[2] S. Duscha,[2] J. Eislöffel,[20] D. Engels,[21] H. Falcke,[2,18] R. A. Fallows,[2] R. Fender,[22] C. Ferrari,[23] W. Frieswijk,[2] M. A. Garrett,[2,24] J. Grießmeier,[25,26] A. W. Gunst,[2] T. E. Hassall,[17] G. Heald,[2] M. Hoeft,[20] J. Hörandel,[18] M. Iacobelli,[24] E. Juette,[27] V. I. Kondratiev,[2,28] M. Kuniyoshi,[29] G. Kuper,[2] G. Mann,[11] S. Markoff,[30] R. McFadden,[2] D. McKay-Bukowski,[31,32] J. P. McKean,[1,2] D. D. Mulcahy,[29] H. Munk,[2] A. Nelles,[18] M. J. Norden,[2] E. Orru,[2] M. Pandey-Pommier,[33] R. Pizzo,[2] A. G. Polatidis,[2] W. Reich,[29] A. Renting,[2] H. Röttgering,[24] D. Schwarz,[34] A. Shulevski,[1] O. Smirnov,[4,5] B. W. Stappers,[35] M. Steinmetz,[11] J. Swinbank,[30] M. Tagger,[25] Y. Tang,[2] C. Tasse,[36] S. ter Veen,[18] S. Thoudam,[18] C. Toribio,[2] C. Vocks,[11] M. W. Wise,[2,30] O. Wucknitz[29] and P. Zarka[36]

Affiliations are listed at the end of the paper

Accepted 2015 April 2. Received 2015 March 30; in original form 2014 July 13

ABSTRACT

We present radio observations of the Moon between 35 and 80 MHz to demonstrate a novel technique of interferometrically measuring large-scale diffuse emission extending far beyond the primary beam (global signal) for the first time. In particular, we show that (i) the Moon appears as a negative-flux source at frequencies $35 < \nu < 80$ MHz since it is 'colder' than the diffuse Galactic background it occults, (ii) using the (negative) flux of the lunar disc, we can reconstruct the spectrum of the diffuse Galactic emission with the lunar thermal emission as a reference, and (iii) that reflected RFI (radio-frequency interference) is concentrated at the centre of the lunar disc due to specular nature of reflection, and can be independently measured. Our RFI measurements show that (i) Moon-based Cosmic Dawn experiments must design for an Earth-isolation of better than 80 dB to achieve an RFI temperature <1 mK, (ii) Moon-reflected RFI contributes to a dipole temperature less than 20 mK for Earth-based

⋆ E-mail: harish@astro.rug.nl

© 2015 The Authors
Published by Oxford University Press on behalf of the Royal Astronomical Society

Cosmic Dawn experiments, (iii) man-made satellite-reflected RFI temperature exceeds 20 mK if the aggregate scattering cross-section of visible satellites exceeds 175 m^2 at 800 km height, or 15 m^2 at 400 km height. Currently, our diffuse background spectrum is limited by sidelobe confusion on short baselines (10–15 per cent level). Further refinement of our technique may yield constraints on the redshifted global 21 cm signal from Cosmic Dawn ($40 > z > 12$) and the Epoch of Reionization ($12 > z > 5$).

Key words: methods: observational – techniques: interferometric – Moon – dark ages, reionization, first stars.

1 INTRODUCTION

The cosmic radio background at low frequencies (<200 MHz) consists of Galactic and extragalactic synchrotron and free–free emission (hundreds to thousands of kelvin brightness) and a faint (millikelvin level) redshifted 21 cm signal from the dark ages ($1100 > z > 40$), Cosmic Dawn ($40 > z > 15$), and the Epoch of Reionization ($15 > z > 5$). The redshifted 21 cm signal from Cosmic Dawn and the Epoch of Reionization is expected to place unprecedented constraints on the nature of the first stars and black holes (Furlanetto, Oh & Briggs 2006; Pritchard & Loeb 2010). To this end, many low-frequency experiments are proposed, or are underway: (i) interferometric experiments that attempt to measure the spatial fluctuations of the redshifted 21 cm signal, and (ii) single-dipole (or total power) experiments that attempt to measure the sky-averaged (or global) brightness of the redshifted 21 cm signal.

An accurate single-dipole (all-sky) spectrometer can measure the cosmic evolution of the global 21 cm signal, and place constraints on the onset and strength of Ly α flux from the first stars and X-ray flux from the first accreting compact objects (Mirocha, Harker & Burns 2013). However, Galactic foregrounds in all-sky spectra are expected to be 4–5 orders of magnitude brighter than the cosmic signal. Despite concerted efforts (Chippendale 2009; Harker et al. 2012; Rogers & Bowman 2012; Patra et al. 2013; Voytek et al. 2014), accurate calibration to achieve this dynamic range remains elusive. Single-dipole spectra are also contaminated by receiver noise which has non-thermal components with complex frequency structure that can confuse the faint cosmic signal. The current best upper limits on the 21 cm signal from Cosmic Dawn comes from the SCI-HI group, who reported systematics in data at about 1–2 orders of magnitude above the expected cosmological signal (Voytek et al. 2014). In this paper, we take the first steps towards developing an alternate technique of measuring an all-sky (or global) signal that circumvents some of the above challenges.

Multi-element telescopes such as LOFAR (van Haarlem et al. 2013) provide a large number of constraints to accurately calibrate individual elements using bright compact astrophysical sources that have smooth synchrotron spectra. Moreover, interferometric data contains correlations between electric fields measured by independent receiver elements, and is devoid of receiver noise bias. These two properties make interferometry a powerful and well-established technique at radio frequencies (Thompson, Moran & Swenson 2007). However, interferometers can only measure fluctuations in the sky brightness (on different scales) and are insensitive to a global signal. However, lunar occultation introduces spatial structure on an otherwise featureless global signal. Interferometers are sensitive to this structure, and can measure a global signal with the lunar brightness as a reference (Shaver et al. 1999). At radio frequencies, the Moon is expected to be a spectrally featureless blackbody (Heiles & Drake 1963; Krotikov & Troitskii 1963) making it an effective temperature reference. Thus, lunar occultation allows us to use the desirable properties of interferometry to accurately measure a global signal that is otherwise inaccessible to traditional interferometric observations.

The first milestone for such an experiment would be a proof of concept, wherein one detects the diffuse or global component of the Galactic synchrotron emission by interferometrically observing its occultation by the Moon. McKinley et al. (2013) recently lead the first effort in this direction at higher frequencies ($80 < \nu < 300$ MHz) corresponding to the Epoch of Reionization. However, McKinley et al. (2013) concluded that the apparent temperature of the Moon is contaminated by reflected man-made interference (or earthshine) – a component they could not isolate from the Moon's intrinsic thermal emission, and hence, they could not estimate the Galactic synchrotron background spectrum.

In this paper, we present the first radio observations of the Moon at frequencies corresponding to the Cosmic Dawn ($35 < \nu < 80$ MHz; $40 > z > 17$). We show that (i) the Moon appears as a source with negative flux density (~ -25 Jy at 60 MHz) at low frequencies as predicted, (ii) that reflected earthshine is mostly specular in nature, due to which, it manifests as a compact source at the centre of the lunar disc, and (iii) that reflected earthshine can be isolated as a point source, and removed from lunar images using the resolution afforded by LOFAR's long baselines (>100λ). Consequently, by observing the lunar occultation of the diffuse radio sky, we demonstrate simultaneous measurement of the spectrum of (a) diffuse Galactic emission and (b) the earthshine reflected by the Moon. These results demonstrate a new and exciting observational channel for measuring large-scale diffuse emission interferometrically.

The rest of the paper is organized as follows. In Section 2, we describe the theory behind extraction of the brightness temperature of diffuse emission using lunar occultation. In Section 3, we present the pilot observations, data reduction, and lunar imaging pipelines. In Section 4, we demonstrate modelling of lunar images for simultaneous estimation of the spectrum of (i) reflected earthshine flux, and (ii) the occulted Galactic emission (global signal). We then use the earthshine estimates to compute limitations to Earth and Moon-based single-dipole Cosmic Dawn experiments. Finally, in Section 5, we present the salient conclusions of this paper, and draw recommendations for future work.

2 LUNAR OCCULTATION AS SEEN BY A RADIO INTERFEROMETER

As pointed out by Shaver et al. (1999), the Moon may be used in two ways to estimate the global 21 cm signal. First, since the Moon behaves as a ∼230-K thermal blackbody at radio frequencies (Heiles & Drake 1963; Krotikov & Troitskii 1963), it can be used in place of a man-made temperature reference for bandpass calibration of single-dish telescopes. Secondly, the Moon can aid in an interferometric measurement of the global signal, which in the absence of the Moon would be resolved out by the interferometer baselines.

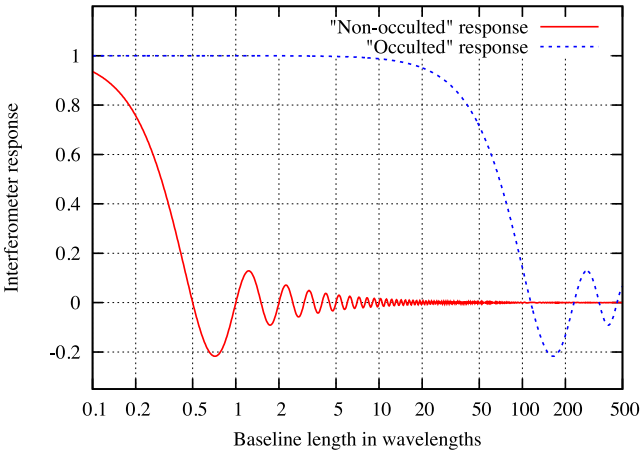

Figure 1. Normalized response of an interferometer to lunar occultation as a function of baseline length: the blue broken line shows the 'occulted' component (equation 7) and the solid red line shows the 'non-occulted' component (equation 6). The solid red line is also the interferometer response in the absence of occultation.

In this section, we describe the theory and intuition behind this quirk of radio interferometry. For simplicity, we will assume that the occulted sky is uniformly bright (global signal only), and that the primary beam is large compared to the Moon, so that we can disregard its spatial response.

2.1 Interferometric response to a global signal

A radio interferometer measures the spatial coherence of the incident electric field. We denote this spatial coherence, also called visibility, at frequency ν, on a baseline separation vector $\bar{u}$ (in wavelength units) as $V(\bar{u}, \nu)$. The spatial coherence function $V(\bar{u}, \nu)$ is related to the sky brightness temperature $T(\bar{r}, \nu)$ through a Fourier transform given by (Thompson et al. 2007)

$$V(\bar{u}, \nu) = \frac{1}{4\pi} \int \mathrm{d}\Omega\, T_{\rm sky}(\bar{r}, \nu)\, \mathrm{e}^{-2\pi \mathrm{i} \bar{u}.\bar{r}}, \tag{1}$$

where $\bar{r}$ is the unit vector denoting direction on the sky, and $\mathrm{d}\Omega$ is the differential solid angle, and we have assumed an isotropic antenna response. Note that we have expressed the visibility in terms of brightness temperature rather than flux density, since brightness temperature gives a more intuitive understanding of a diffuse signal such as the global 21 cm signal as compared to the flux density which lends itself to representation of emission from compact sources.

If the sky is uniformly bright as in the case of a global signal, then[1] $T_{\rm sky}(\bar{r}, \nu) = T_{\rm B}(\nu)$, and by using a spherical harmonic expansion of the integrand in equation (1), we can show that (full derivation in Appendix A)

$$V(\bar{u}, \nu) = T_{\rm B}(\nu)\, \frac{\sin(2\pi|\bar{u}|)}{2\pi|\bar{u}|}, \tag{2}$$

where $|\bar{u}|$ is the length of vector $\bar{u}$. Equation (2) implies that the response of an interferometer with baseline vector $\bar{u}$ (in wavelengths) to a global signal (no spatial structure) falls off as $\sim 1/|\bar{u}|$. Hence only a zero baseline, or very short baselines ($<$ few λ) are sensitive to a global signal. This is seen in Fig. 1 (solid red curve) where we plot the interferometric response to a global signal as given by equation (2).

In zero-baseline (single-dipole) measurements, the signal is contaminated by receiver noise which is very difficult to measure or model with accuracy ($\sim$10 mK level). This is evident from recent efforts by Chippendale (2009), Rogers & Bowman (2012), Harker et al. (2012), Patra et al. (2013), and Voytek et al. (2014). On shorter non-zero baselines, the receiver noise from the two antennas comprising the baseline, being independent, has in principle, no contribution to the visibility $V(\bar{u})$. In practice however, short baselines ($<$ few wavelengths) are prone to contamination from mutual coupling between the antenna elements, which is again very difficult to model. Moreover, non-zero baselines are also sensitive to poorly constrained large-scale Galactic foregrounds and may not yield accurate measurements of a global signal.

2.2 Response to occultation

The presence of the Moon in the field of view modifies $T_{\rm sky}(\nu)$. If the lunar brightness temperature is $T_{\rm M}(\nu)$ and the global brightness temperature in the field is $T_{\rm B}(\nu)$, then lunar occultation imposes a disc-like structure of magnitude $T_{\rm M}(\nu) - T_{\rm B}(\nu)$ on an otherwise featureless background.

To mathematically represent the occultation, we introduce the masking function which is unity on a disc the size of the Moon ($\sim$0.5 deg) centred on the Moon at $\bar{r}_{\rm M}$, and zero everywhere:

$$M(\bar{r}, \bar{r}_{\rm M}) = \left\{ \begin{array}{ll} 1 & \bar{r}.\bar{r}_{\rm M} > \cos(0.25\,\mathrm{deg}) \\ 0 & \text{otherwise.} \end{array} \right\}. \tag{3}$$

The sky brightness may then be expressed as,

$$\begin{aligned} T_{\rm sky} &= T_{\rm B}\,(1 - M) + T_{\rm M}\, M \\ &= \underbrace{(T_{\rm M} - T_{\rm B})M}_{\rm occulted} + \underbrace{T_{\rm B}}_{\rm non-occulted}, \end{aligned} \tag{4}$$

where the function arguments have been dropped for brevity. Equation (4) shows that $T_{\rm sky}$ consists of (i) a spatially fluctuating 'occulted' component:[2] $(T_{\rm M} - T_{\rm B})M$, and (ii) a spatially invariant 'non-occulted' component: $T_{\rm B}$ akin to the occultation-less case discussed in Section 2.1. By substituting equation (4) in equation (1), we get an expression for the visibility:

$$\begin{aligned} V(\bar{u}) = &\underbrace{\frac{1}{4\pi}(T_{\rm M} - T_{\rm B}) \int \mathrm{d}\Omega\, M(\bar{r}, \bar{r}_{\rm M})\, \mathrm{e}^{-2\pi \mathrm{i} \bar{u}.\bar{r}}}_{\rm occulted} \\ &+ \underbrace{\frac{1}{4\pi} T_{\rm B} \int \mathrm{d}\Omega\, \mathrm{e}^{-2\pi \mathrm{i} \bar{u}.\bar{r}}}_{\rm non-occulted}. \end{aligned} \tag{5}$$

The above equation is central to the understanding of the occultation-based technique presented in this paper. The second integral representing the 'non-occulted' brightness evaluates to a sinc-function (see equation 2):

$$V_2(\bar{u}) = T_{\rm B}\, \frac{\sin(2\pi|\bar{u}|)}{2\pi|\bar{u}|} \quad \text{(non-occulted)}. \tag{6}$$

This is the interferometric response we expect in the absence of any occultation.

[1] In this context, we use $T_{\rm B}(\nu)$ to denote a generic spatially invariant function – not necessarily the particular case of the global 21 cm signal.

[2] Though $T_{\rm B}$ and $T_{\rm M}$ are assumed here to have no spatial fluctuations, $(T_{\rm M} - T_{\rm B})M$ has spatial fluctuations due to M.

The first integral is the additional term generated by the occultation. It is a measure of $T_B - T_M$: the differential brightness temperature between the background being occulted and the occulting object itself. This integral is simply the Fourier transform of a unit disc, and if we (i) assume that the angular size of the occulting object, a is small, and (ii) use a coordinate system which has its z-axis along $\bar{r}_M$, then it reduces to the well-known Airy-pattern:

$$V_1(\bar{u}) \approx (T_M - T_B)\frac{\Omega_a}{4\pi}\frac{2J_1(\pi a|\bar{u}|)}{\pi a|\bar{u}|} \text{ (occulted)}, \quad (7)$$

where Ω_a is the beam-solid angle of the occulting object, and J_1 is the Bessel function of the first kind of order 1. This is the additional interferometric response due to the presence of the occulting object.

In Fig. 1, we plot the interferometric response to the 'occulted' and 'non-occulted' components as a function of baseline length for $a = 0.5$ deg. Clearly, longer baselines ($|\bar{u}| \sim 1/a$) of a few tens of wavelengths are sensitive to the 'occulted' component $T_M - T_B$. With prior knowledge of T_M, the global background signal T_B may be recovered from these baselines. The longer baselines also have two crucial advantages: (i) they contain negligible mutual coupling contamination, and (ii) they probe scales on which Galactic foreground contamination is greatly reduced as compared to very short baselines (few wavelengths). These two reasons are the primary motivations for the pilot project presented in this paper.

2.3 Lunar brightness: a closer look

Since an interferometer measures $T_M - T_B$, our recovery of T_B hinges on our knowledge of T_M. We have thus far assumed that the lunar brightness temperature, T_M, is given by a perfect blackbody spectrum without spatial structure. In practice, the apparent lunar temperature consists of several non-thermal contributions. We now briefly discuss these in decreasing order of significance.

(i) *Reflected RFI:* Man-made interference can reflect off the lunar disc into the telescope contributing to the effective lunar temperature. Radar studies have shown that the lunar surface appears smooth and undulating at wavelengths larger than ∼5 m (Evans 1969). Consequently, at frequencies of interest to Cosmic Dawn studies ($35 < \nu < 80$ MHz) earthshine reflection is expected to be specular in nature and may be isolated by longer baselines ($>100\,\lambda$) to the centre of the lunar disc. This 'reflected earthshine' was the limiting factor in recent observations by McKinley et al. (2013). In Section 4, we demonstrate how the longer baselines of LOFAR ($>100\,\lambda$) can be used to model and remove earthshine from images of the Moon.

(ii) *Reflected Galactic emission:* The Moon also reflects Galactic radio emission incident on it. As argued before, the reflection at tens of MHz frequencies is mostly specular. Radar measurements of the dielectric properties of the lunar regolith have shown that the Moon behaves as a dielectric sphere with an albedo of ∼7 per cent (Evans 1969). If the sky were uniformly bright (no spatial structure) this would imply an additional lunar brightness of $0.07\,T_B(\nu)$ K, leading to a simple correction to account for this effect. In reality, Galactic synchrotron has large-scale structure (due to the Galactic disc) and the amount of reflected emission depends on the orientation of the Earth–Moon vector with respect to the Galactic plane and changes with time. For the sensitivity levels we reach with current data (see Section 4.1), it suffices to model reflected emission as a time-independent temperature of 160 K at 60 MHz with a spectral index of −2.24:

$$T_{refl} = 160\left(\frac{\nu\ \text{MHz}}{60}\right)^{-2.24}. \quad (8)$$

Details of simulations that used the sky model from de Oliveira-Costa et al. (2008) to arrive at the above equation are presented in Appendix B.

(iii) *Reflected solar emission:* The radio-emitting region of the quiet Sun is about 0.7 deg in diameter, has a disc-averaged brightness temperature of around 10^6 K at our frequencies, and has a power-law-like variation with frequency (Erickson et al. 1977). Assuming specular reflection, the reflected solar emission from the Moon is localized to a 7-arcsec wide region on the Moon, and as such can be modelled and removed. In any case, assuming an albedo of 7 per cent, this adds a contribution of about 1 K to the disc-integrated temperature of the Moon. While this contribution must be taken into account for 21 cm experiments, we currently have not reached sensitivities where this is an issue. For this reason, we discount reflected solar emission from the quiet Sun in this paper. During disturbed conditions, transient radio emission from the Sun may increase by ∼4 orders of magnitude and have complex frequency structure. According to SWPC,[3] such events were not recorded during the night in which our observations were made.

(iv) *Polarization:* The reflection coefficients for the lunar surface depend on the polarization of the incident radiation. For this reason both the thermal radiation from the Moon, and the reflected Galactic radiation is expected to be polarized. Moffat (1972) has measured the polarization of lunar thermal emission to have spatial dependence reaching a maximum value of about 18 per cent at the limbs. While leakage of polarized intensity into Stokes I brightness due to imperfect calibration of the telescopes is an issue for deep 21 cm observations, we currently do not detect any polarized emission from the lunar limb in our data. The most probable reason for this is depolarization due to varying ionospheric rotation measure during the synthesis, and contamination from imperfect subtraction of a close (∼5 deg), polarized, and extremely bright source (Crab pulsar).

In this paper, we model the lunar brightness temperature as a sum of its intrinsic blackbody emission, and reflected emission:

$$T_M = T_{black} + T_{refl} = 230 + 160\left(\frac{\nu\ \text{MHz}}{60}\right)^{-2.24}\ \text{K} \quad (9)$$

The top panel in Fig. 2 shows the expected diffuse background T_B, and the above two contributions to the lunar brightness temperature T_M as a function of frequency assuming that the Moon is located at $05^h13^m00^s$, $+20^\circ26'00''$.[4] The bottom panel of Fig. 2 also shows the flux density of the lunar disc S_m (Stokes I) given by

$$S_m = \frac{2k(T_M - T_B)\Omega}{\lambda^2 10^{-26}}\ \text{Jy}, \quad (10)$$

where the temperatures are expressed in kelvin, k is the Boltzmann's constant, λ is the wavelength, and Ω is the solid angle subtended by the Moon. Since $T_M - T_B$ is negative in our frequency range, the Moon is expected to appear as a negative source with flux density of about −25 Jy at 60 MHz. In Section 4.3, we will use equations (10)

[3] National Oceanic and Atmospheric Administration's Space Weather Prediction Center (http://www.swpc.noaa.gov).

[4] This corresponds to the transit point of the Moon during the observations presented in this paper.

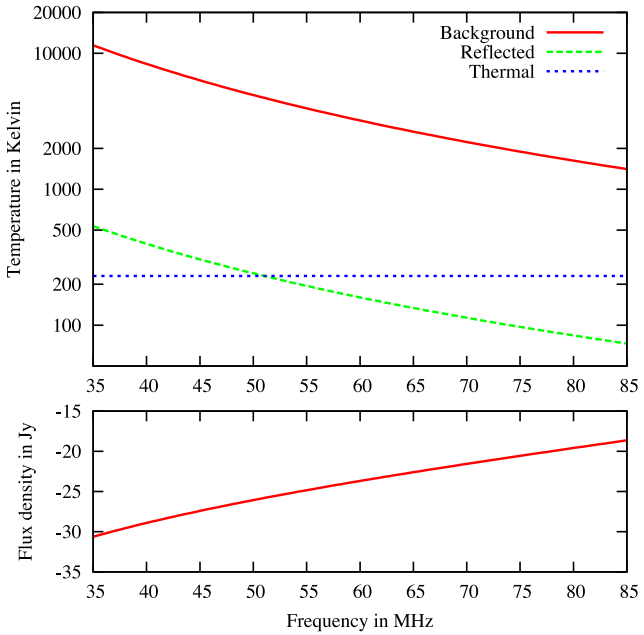

Figure 2. Plot showing the expected temperature of occulted Galactic synchrotron emission, reflected Galactic emission, and lunar thermal emission as a function of frequency (top panel), and also the resulting flux density of the Moon as measured by an interferometer (bottom panel).

and (9), along with a measurement of the S_m, to compute the spectrum of the diffuse background T_B.

3 PROOF OF CONCEPT

We acquired 7 h of LOFAR (van Haarlem et al. 2013) commissioning data between 26-12-2012 19:30 UTC and 27-12-2012 02:30 UTC. 24 low-band antenna (LBA) core-stations (on a common clock) and 11 remote stations participated in the observation.[5] The core-stations are distributed within a ∼3 km core near the town of Exloo in the Netherlands, and the remote stations are distributed up to ∼50 km away from the core within the Netherlands. Visibility data were acquired in two simultaneous (phased array) primary beams : (i) a calibration beam on 3C123 ($04^h37^m04^s$, $+29^\circ40'13\farcs8$), and (ii) a beam in the direction of the Moon at transit ($05^h13^m, +\ 20^\circ26'$).[6] We acquired data on the same 244 sub-bands (each ∼195 kHz wide) in both beams. These sub-bands together span a frequency range from ∼36 to ∼83.5 MHz. The raw data were acquired at a time/frequency resolution of 1 s, 3 kHz (64 channels per sub-band) to reduce data loss to radio-frequency interference (RFI), giving a raw-data volume of about 15 TB.

3.1 RFI flagging and calibration

RFI ridden data points were flagged using the `AOFlagger` algorithm (Offringa et al. 2013) in both primary (phased-array) beams. The 3C123 calibrator beam data were then averaged to 5 s, 195 kHz (1 channel per sub-band) resolution such that the clock-drift errors on the remote stations could still be solved for. We then bandpass calibrated the data using a two component model for 3C123. The bandpass solutions for the core-station now contain both instrumental gains and ionospheric phases in the direction of 3C123. Since 3C123 is about 12 deg from the Moon, the ionospheric phases may not be directly translated to the lunar field. To separate instrumental gain and short-term ionospheric phase, we filtered the time series of the complex gains solutions in the Fourier domain (low-pass) and then applied them to the lunar field. Since the baselines sensitive to the occultation signal ($<100\lambda$) are well within typical diffractive scales for ionospheric phase fluctuations (few km), to first order, we do not expect significant ionospheric corruptions in the measurement of the occultation response.

3.2 Subtracting bright sources

The brightest source in the lunar field is 3C144 which is about 5 deg from the pointing centre (see Fig. 4). 3C144 consists of a pulsar (250 Jy at 60 MHz) and a nebula (2000 Jy at 60 MHz) which is around 4 arcmin wide. After RFI flagging, the lunar field data were averaged to 2 s, 13 kHz (15 channel per sub-band). This ensures that bright sources away from the field such as Cassiopeia A are not decorrelated, such that we may solve in their respective directions for the primary beam and ionospheric phase, and remove their contribution from the data. We used the third Cambridge Catalogue (Bennett 1962) with a spectral index scaling of $\alpha = -0.7$, in conjunction with a nominal LBA station beam model to determine the apparent flux of bright sources in the lunar beam at 35, 60, and 85 MHz (see Fig. 3). Clearly, 3C144 (Crab nebula) and 3C461 (Cassiopeia A) are the dominant sources of flux in the lunar beam across the observation bandwidth. Consequently, we used the BlackBoard Self-cal (BBS[7]) software package to calibrate in the direction of Cassiopeia A, and the Crab nebula simultaneously, and also subtract them from the data. We used a Gaussian nebula plus point-source pulsar model for the Crab nebula, and a two component Gaussian model for Cassiopeia A in the solution and subtraction process.

3.3 Faint source removal

Since the Moon is a moving target (in celestial coordinates), all the background sources and their sidelobes will be spatially smeared in lunar images. Standard imaging routines cannot clean (deconvolve) the sidelobes of such spatially smeared sources. To mitigate sidelobe confusion, it is thus important to model and subtract as many background sources as possible prior to lunar imaging. After removing the bright sources, Cassiopeia A and the Crab nebula, we average the data to a resolution of 10 s, 40 kHz (5 channel per sub-band) to ensure that the faint sources that populate the relatively large beam (full width at half maximum of ∼20 deg at 35 MHz) are not decorrelated from time and bandwidth smearing, such that they may be reliably subtracted. We then imaged the sources and extracted a source catalogue consisting of ∼200 sources in the field (see Fig. 4). Since the time-variable LOFAR primary-beam attenuation towards these sources is not well known, we are unable to directly peel the catalogued sources from the visibilities. We instead spatially clustered these sources into 10–12 directions depending on frequency, and used the SAGECAL software (Kazemi et al. 2011) to solve for the time-varying primary beam in the direction of each

[5] Station here refers to a phased array of dipoles that forms the primary antenna element in the interferometer.

[6] All coordinates are specified for equinox J2000 at epoch J2000, but for lunar coordinates that are specified for equinox J2000 at epoch J2012 December 26 23:00 UTC.

[7] BBS is a self-calibration software package developed for LOFAR

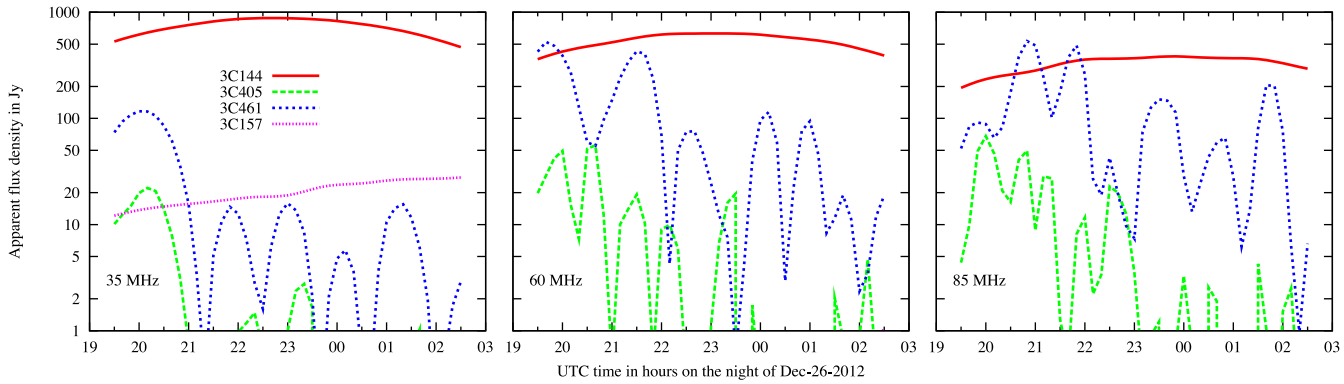

Figure 3. Plot showing the simulated apparent flux (primary-beam attenuated) of sources which dominate the flux budget in the lunar field for three different frequencies: 35, 60, and 80 MHz. The modulations in time are due to the sources moving through the sidelobes of the primary (station) beam during the synthesis.

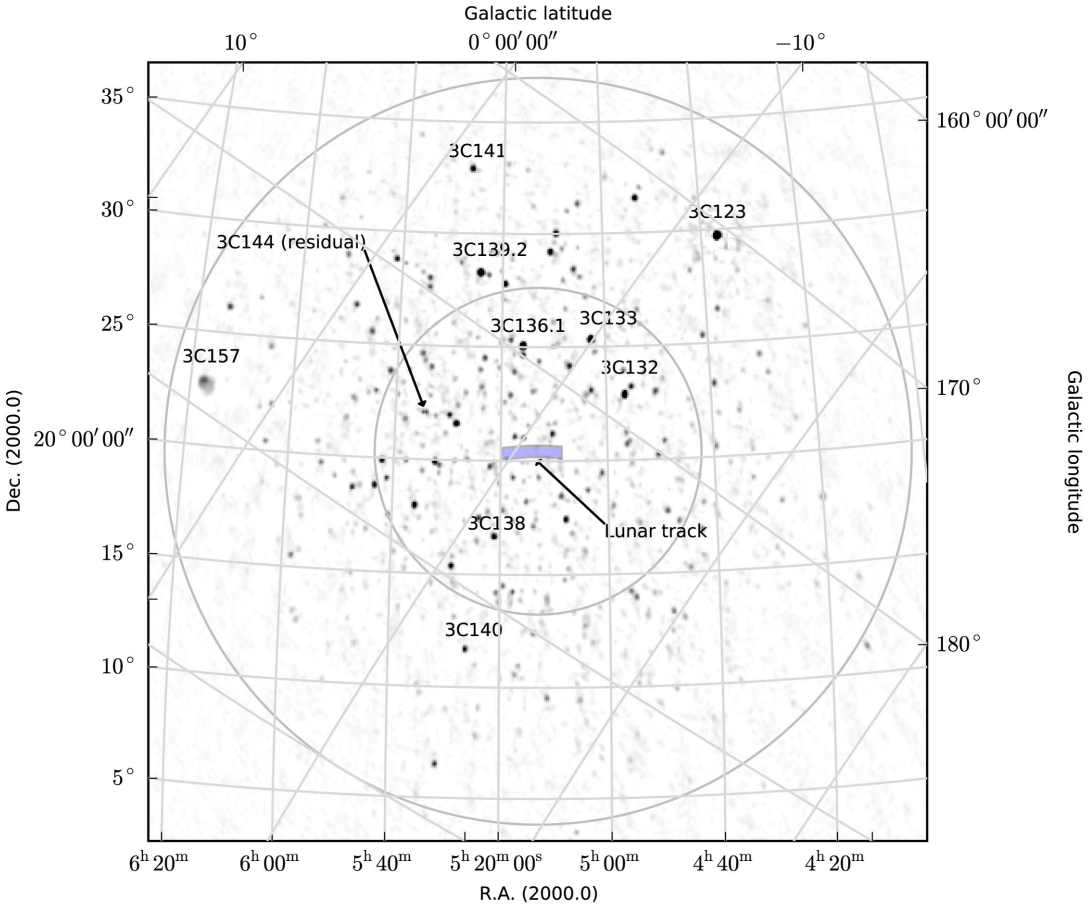

Figure 4. Continuum image of the lunar field between 36 and 44 MHz (natural weights) with no primary-beam correction applied. The point spread function is about 12 arcmin wide. Prominent 3C source names have been placed right above the respective sources. 3C144 (Crab nebula) has been subtracted in this image. The grey circles approximately trace the first null of the primary beam at 35 (outer) and 80 MHz (inner). The shaded rectangular patch shows the trajectory of the Moon during the 7 h synthesis. We have not fringe-stopped on the Moon (moving source) in producing this image, and hence the Moon is not visible due to the ensuing decorrelation.

cluster with a solution cadence of 40 min. SAGECAL is a radio interferometric self-calibration algorithm that uses a clustered sky-model to estimate (direction dependent) antenna-based gains towards each cluster. Using these gain solutions, the catalogued sources were subtracted from the visibilities. Note that the SAGECAL solutions were not applied to the visibilities (post subtraction). The residual visibilities are unaffected by inaccuracies in the absolute fluxes in our sky model so long as the relative fluxes of the sources within a cluster are accurate: inaccuracies in the absolute flux are absorbed into the cluster-dependant gain solutions. We also note here that none of the sources detected for the 200 source catalogue were occulted by the Moon. In future experiments, if bright sources are occulted

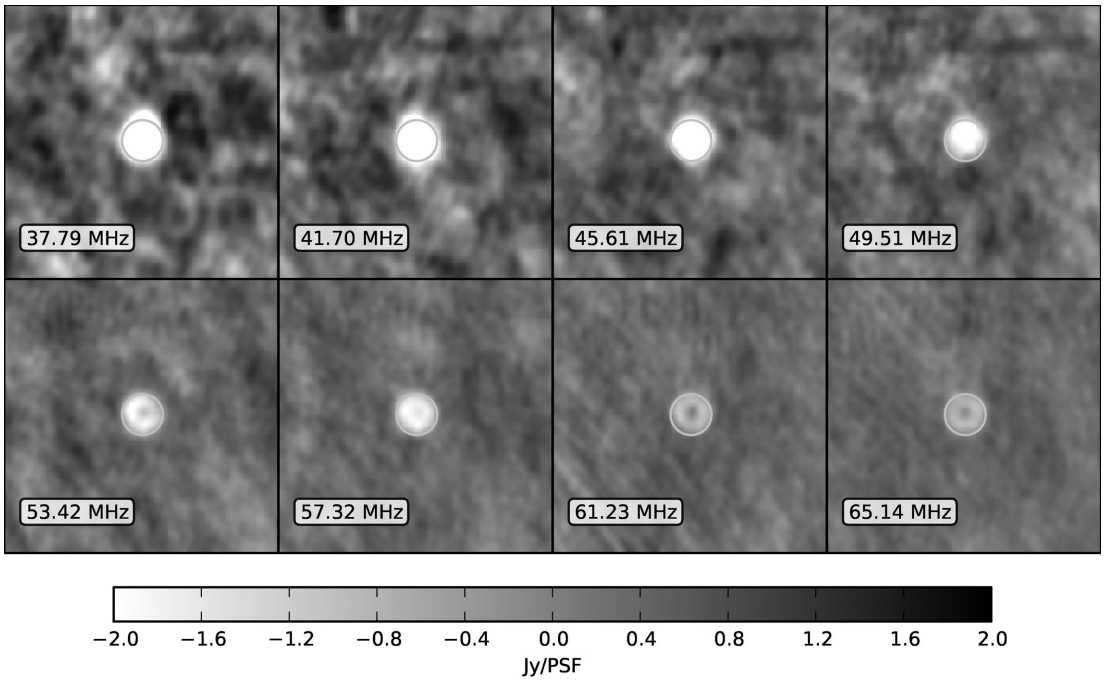

Figure 5. Synthesis images of the Moon at eight different frequencies: 0.5 deg wide grey circles are drawn centred on the expected position of the Moon. Each image is made over a bandwidth of 3.9 MHz (20 sub-bands) for 7 h of synthesis. The lunar flux increases towards zero with increasing frequency as the contrast between the Galactic background and lunar thermal emission is decreasing (as expected).

by the Moon during the synthesis, then care must be exercised to (i) not subtract them during the occultation, and (ii) flag data at the beginning and end of occultation that contains edge diffraction effects.

Multidirection algorithms may subtract (or suppress) flux from sources that are not included in the source model in their quest to minimize the difference between data and model (Kazemi & Yatawatta 2013; Grobler et al. 2014). Furthermore, the Moon is a moving source (in the celestial coordinates frame in which astrophysical sources are fixed). The Moon fringes on a 100λ east–west baseline at a rate of about 360 deg h^{-1}. Based on fringe rate alone, such a baseline will confuse the Moon for a source that is a few degrees from the phase centre that also fringes at the same rate. This implies that calibration and source subtraction algorithms are expected to be even more prone to subtracting lunar flux due to confusion with other sources in the field. While a discussion on the magnitude of these effects are beyond the scope of this paper, to mitigate these effects, we excluded all baselines less than 100λ (that are sensitive to the Moon) in the SAGECAL solution process to avoid suppressing flux from the Moon, and also to avoid confusion from the unmodelled diffuse Galactic emission.

3.4 Lunar imaging

After faint source removal, the data were averaged to a resolution of 1 min, 195 kHz (1 channel per sub-band) to reduce data volume while avoiding temporal decorrelation of the Moon (moving target). We then phase rotated (fringe stopping) to the Moon while taking into account its position and parallax given LOFAR's location at every epoch. After this step, we used standard imaging routines in CASA to make a dirty image of the Moon. Since we are primarily interested in the spectrum of lunar flux in images, it is critical to reduce frequency-dependent systematics in the images. As shown later, sidelobe confusion on short baselines (<100λ) is the current limitation in our data. This contamination is a result of the frequency-dependent nature of our native UV-coverage – an indispensable aspect of Fourier synthesis imaging. To mitigate this effect on shorter baselines, we choose an inner UV-cut of 20λ for all frequency channels. This value was chosen as it corresponds to the shortest baselines (in wavelengths) available at the highest frequencies in our observation bandwidth. Fig. 5 shows 3.9 MHz wide (20 sub-bands) continuum images of the Moon in different frequency bands. As expected the Moon appears as a source with negative flux density. As frequency increases, the brightness contrast between the Moon and the background Galactic emission decreases, and the (absolute) flux of the Moon decreases, just as expected.

4 IMAGE ANALYSIS

In this section, we use the lunar images such as the ones shown in Fig. 5 to extract the background temperature T_B and the reflected RFI (earthshine) flux.

4.1 Sensitivity analysis

The noise in lunar images such as the ones in Fig. 5 primarily originate from (i) thermal noise, (ii) classical and sidelobe confusion noise, and (iii) residuals of the bright in-field source 3C144 (about 2250 Jy at 60 MHz).[8] To estimate thermal noise, we differenced the bandpass-calibrated visibilities on a single baseline between channels separated by 40 kHz. The aggregated flux from sources across the sky are correlated on such a small frequency interval (0.01 per cent), and drop off in the difference. After taking into account the frequency and time resolution of the visibilities, the rms of the differenced visibilities gives us an independent measurement

[8] The dirty images of unsubtracted sources are spatially smeared in lunar images since we have fringe stopped on the Moon.

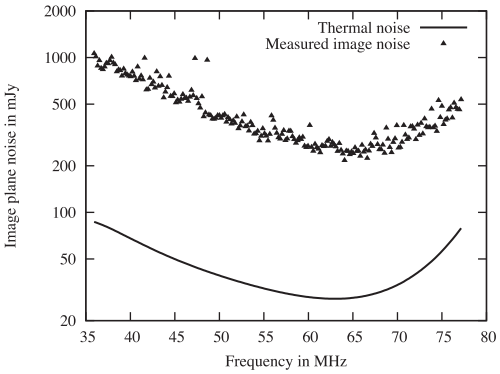

Figure 6. Plot showing noise estimated in the lunar images. The thermal noise was estimated by differencing visibilities between frequency channels separated by about 40 kHz. The measured image noise is shown for naturally weighted images (20λ–500λ baselines) made over a bandwidth of about 195 kHz with a 7 h synthesis.

of the system equivalent flux density (SEFD). From the SEFD, we compute the thermal noise in natural weighted images as

$$\sigma_{\rm th}(\nu) = \frac{\rm SEFD(\nu)}{\sqrt{2\, t_{\rm syn}\, \Delta\nu\, N_{\rm bas}}}, \tag{11}$$

where $t_{\rm syn}$ is the observation duration, $\Delta\nu$ is the bandwidth, and $N_{\rm bas}$ is the number of baselines used in imaging. Fig. 6 shows the expected thermal noise in lunar images (solid black line). The thermal noise is sky limited for $\nu < 65$ MHz, and receiver noise begins to become a significant contributor at higher frequencies. Fig. 6 also shows the measured rms noise in Stokes I lunar images (solid triangles), which is a factor of 6–12 times (frequency dependent) higher than the thermal noise alone. The expected confusion noise is about 15 mJy at 60 MHz and increases to about 50 mJy at 35 MHz, and cannot account for the excess. Simulations of the effects of 3C sources outside the field of view yielded a sidelobe noise of about 100 mJy at 60 MHz, which may account for no more than a third of the excess. Part of the remaining excess may be due to the residuals of 3C144 which is only about 5 deg from the Moon, scintillating (ionospheric) and extremely bright (2200 Jy at 60 MHz, and 3600 Jy at 35 MHz) and possibly polarized. We currently do not have reliable models to remove its contribution with an error less than 0.5 per cent. Additionally, recent work by Vedantham & Koopmans (2014) shows that speckle noise (or scintillation noise) of all the sources in the field can be significantly larger than thermal noise at low frequencies (<100 MHz). While we are currently unable to pinpoint the exact cause of this excess noise, we defer a detailed sensitivity analysis of the lunar occultation technique to a future paper where we will (i) observe the Moon in a field devoid of extremely bright sources, and (ii) employ internight differencing to cancel (to first order) confusion from sources and their sidelobes (see Section 4.5).

4.2 Mitigating earthshine

The lunar images in certain frequency channels comprise of a negative disc (as expected), along with a bright point-source like emission at the centre of the disc (see for instance the panels corresponding to 61.23 and 65.14 MHz in Fig. 5). Since this point-source like emission is always present only at the centre of the lunar disc, it is not intrinsic to the Moon. Additionally, it cannot emanate from man-made satellites orbiting the Moon, since the apparent positions of man-made satellites must change during the 7 h synthesis. The only known source we may attribute this point-source like emission to is earthshine – man-made RFI reflected off the lunar surface. Since the lunar surface is expected to be smoothly undulating on spatial scales comparable to the wavelength (4–9 m), reflection off the lunar surface is expected to be mostly specular. Hence earthshine always images to the centre of the lunar disc. For specular reflection, the angular size of earthshine in lunar images may be approximately written as (derivation in Appendix C)

$$\Delta\theta_{\rm es} \approx \frac{R_{\rm e}\, R_{\rm m}}{(D - R_{\rm e})^2}, \tag{12}$$

where $R_{\rm e}$ and $R_{\rm m}$ are the radius of the Earth and Moon, respectively, and D is the distance between the Earth and the Moon. The approximation holds for $D \gg R_{\rm m}$ and $D \gg R_{\rm e}$. Assuming approximate values: $R_{\rm e} = 6400$ km, $R_{\rm m} = 1740$ km, $D = 384\,400$ km, we get $\Delta\theta_{\rm es} \approx 16$ arcsec.[9] Additionally, lunar topography results in 'angular broadening' of reflected earthshine. For typical rms slopes of 14 deg on the moon (Daniels 1963), we compute the broadening to be about 3.86 arcmin (derivation in Appendix C). This is still smaller than the 7 arcmin resolution of the largest baselines (500λ) we use in lunar imaging: for the purposes of this paper, we will treat it a point source.

We thus model the dirty lunar images with two components: (i) a lunar disc of 0.5 deg diameter with negative flux $S_{\rm m}$, and (ii) a point source centred on the lunar disc with positive flux, $S_{\rm es}$. If $\mathbf{D}$ is a matrix with dirty image flux values, $\mathbf{M}$ is a mask as defined in equation (3), and $\mathbf{P}$ is the telescope point spread function (PSF) matrix then our model may be expressed as

$$\mathbf{D} = (S_{\rm m}\mathbf{M} + S_{\rm es}) * \mathbf{P} + \mathbf{N}, \tag{13}$$

or equivalently,

$$\mathbf{D} = S_{\rm m}\mathbf{G} + S_{\rm es}\mathbf{P} + \mathbf{N}, \tag{14}$$

where $\mathbf{G} = \mathbf{M} * \mathbf{P}$ is the dirty image of the unit disc given the telescope PSF, and $*$ denotes 2D convolution. The above equation may be vectorized and cast as a linear model with $S_{\rm m}$ and $S_{\rm es}$ are parameters:

$$\mathrm{vec}(\mathbf{D}) = \mathbf{H}\boldsymbol{\theta} + \mathrm{vec}(\mathbf{N}) \tag{15}$$

where

$$\mathbf{H} = [\mathrm{vec}(\mathbf{G})\ \ \mathrm{vec}(\mathbf{P})]$$
$$\boldsymbol{\theta} = [S_{\rm m}\ \ S_{\rm es}]^{\rm T} \tag{16}$$

The maximum-likelihood estimate of the parameters is then

$$\widehat{\boldsymbol{\theta}} = [\widehat{S}_{\rm m}\ \ \widehat{S}_{\rm es}]^{\rm T} = (\mathbf{H}^{\rm T}\mathbf{H})^{-1}\mathbf{H}^{\rm T}\mathrm{vec}(\mathbf{D}), \tag{17}$$

and the residuals of fitting are given by

$$\mathrm{vec}(\mathbf{R}) = \mathrm{vec}(\mathbf{D}) - \mathbf{H}\widehat{\boldsymbol{\theta}}. \tag{18}$$

In practice, we solve equation (17) with a positivity constraint on $\widehat{S}_{\rm es}$, and a negativity constraint on $\widehat{S}_{\rm m}$. Finally, if $\sigma_{\rm N}^2$ is the noise variance, the parameter covariance matrix is given by

$$\mathrm{cov}(\boldsymbol{\theta}) = \sigma_{\rm N}^2(\mathbf{H}^{\rm T}\mathbf{H})^{-1}. \tag{19}$$

Note that we have assumed that the noise covariance matrix is diagonal with identical entries along its diagonal. A more realistic noise covariance matrix may be estimated from autocorrelation of the images themselves, but we found this to lead to marginal change in the

[9] LOFAR's international baselines can achieve sub-arcsecond resolutions. In future, this may be used to make maps of reflected earthshine!

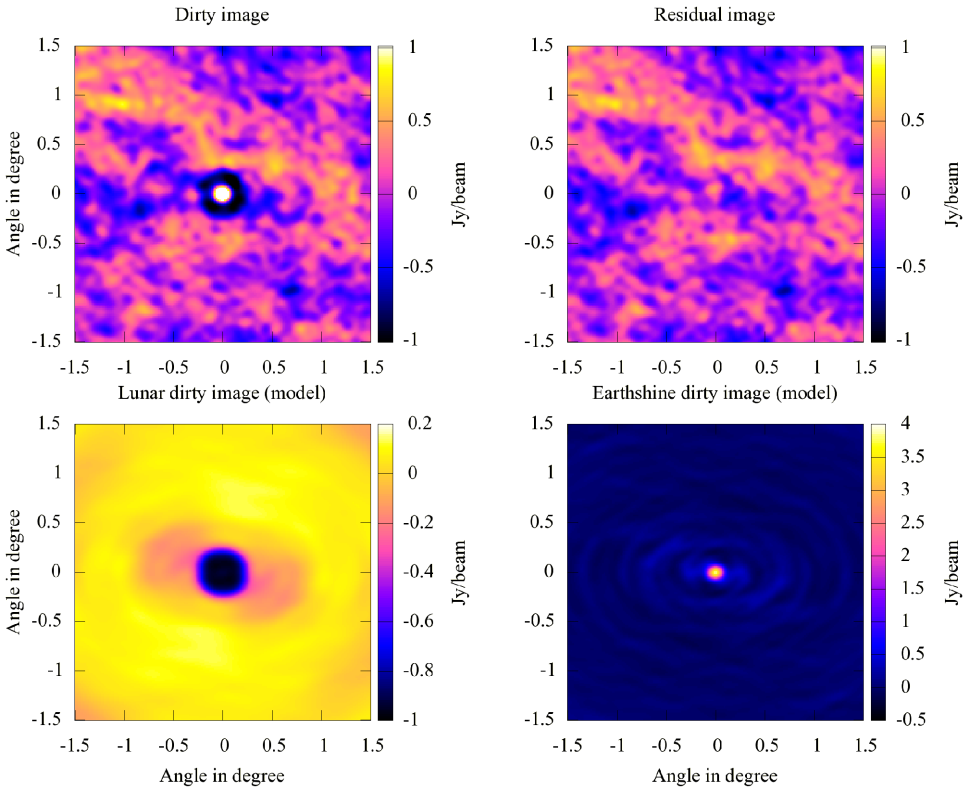

Figure 7. Plot demonstrating the mitigation of reflected RFI (earthshine) in lunar images. Top-left panel shows a dirty image of the Moon at 68 MHz contaminated by earthshine. Bottom-left panel shows the reconstructed dirty image of the Moon with earthshine removed. Bottom-right panel shows the reconstructed dirty image of earthshine only, and top-right panel shows the residuals of model fitting.

background spectrum which is still dominated by larger systematic errors (see Fig. 8).

Fig. 7 demonstrates our modelling procedure on a dirty image of the Moon made with a sub-band strongly contaminated by reflected earthshine. The top-left panel shows the dirty image of the Moon $\mathbf{D}$. The bright positive emission at the centre of the lunar disc is due to reflected earthshine. The bottom-left and bottom-right panels show the reconstruction of the dirty images of the lunar disc alone (given by $\widehat{S}_{\rm m}(\mathbf{M} * \mathbf{P})$, and that of reflected earthshine alone (given by $\widehat{S}_{\rm es}\mathbf{P}$). The top-right panel shows an image of the residuals of fit $\mathbf{R}$. The residual images show non-thermal systematics with spatial structure. This is expected as the noise $\mathbf{N}$ is dominated by sidelobe confusion and residuals of 3C144. Nevertheless, to first order, we have isolated the effect of reflected earthshine from lunar images, and can now estimate the background temperature spectrum independently.

4.3 Background temperature estimation

As shown in Section 2.2, the estimated flux of the lunar disc $\widehat{S}_{\rm m}$ is a measure of the brightness temperature contrast between the Moon and the background: $T_{\rm M} - T_{\rm B}$. Using equations (9) and (10), we get the estimator for the background temperature spectrum as

$$\widehat{T_{\rm B}}(\nu) = 230 + 160\left(\frac{\nu\ {\rm MHz}}{60}\right)^{-2.24} - \frac{10^{-26}c^2\widehat{S}_{\rm m}}{2k\Omega\nu^2}. \qquad (20)$$

Fig. 8 shows the estimates $\widehat{T_{\rm B}}(\nu)$ computed from equation (20) and lunar disc flux estimates $\widehat{S}_{\rm m}(\nu)$ from the fitting procedure described in Section 4.2.

For the data in Fig. 8, we split our 7 h synthesis into seven one-hour syntheses. Hence, for each frequency channel (195 kHz wide), we obtain seven estimates of the occulted brightness temperature. In Fig. 8 we plot the mean (black points) and standard deviation (error bars) of seven temperature estimates at each frequency channel. The actual uncertainties on the estimates (given by equation 19) are significantly smaller than the standard deviation, and hence, we do not show them on this plot. We have applied two minor corrections to the data in Fig. 8: (i) since the Moon moves with respect to the primary-beam tracking point during the synthesis, we apply a net (7 h averaged) primary-beam correction for each frequency using a simple analytical primary-beam model (array factor), and (ii) we bootstrapped the overall flux scale to the 3C123 scale from Perley & Butler (2015). These two corrections only lead to a marginal flattening of the estimated background spectrum, but we include them nevertheless for completeness.

Though the Moon moves by about 0.5 deg h^{-1}, the large hour-to-hour variation seen in our data (error bars in Fig. 8) is likely not intrinsic to the sky, and mostly emanates from sidelobe-confusion noise on short baselines where most of the lunar flux lies. Sidelobes of unsubtracted (or mis-subtracted) sources are also the likely cause of a 10–20 per cent spectral 'ripple' that rides above a smooth power-law-like form in the measured background spectrum of Fig. 8. This is suggested by large angular-scale sidelobe structure that 'moves' across the Moon in images at different frequencies.[10] Due to a lack of accurate models for bright in-field sources (3C144 for instance)

[10] For instance, the observant reader may discern a NW–SE sidelobe structure in Fig. 5.

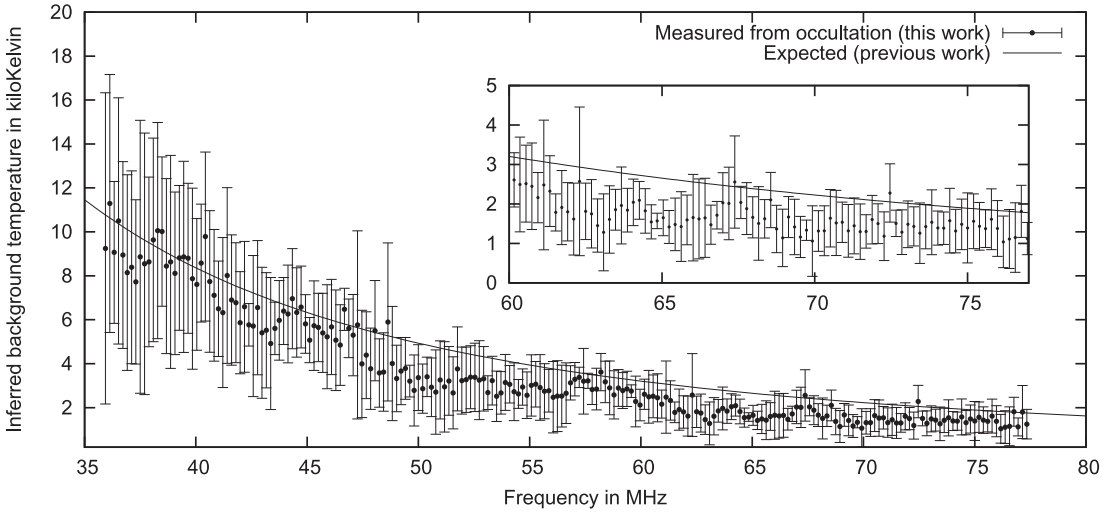

Figure 8. Plot showing the inferred background temperature occulted by the Moon. At each channel, we estimate seven background temperature values using seven one-hour synthesis images of the Moon. Plotted are the mean and standard deviation of the seven temperatures measured in each channel.

and the complex resolved Galactic structure (close to the Galactic plane), we are unable to mitigate this confusion with current data. Regardless, we will not concern ourselves with detailed modelling of this source of systematic error, since as outlined in Section 4.5, we expect to mitigate it in planned internight differencing observations.

Fig. 8 also shows the expected Galactic spectrum from available sky models from de Oliveira-Costa et al. (2008, solid line) which may be approximated by a power law with spectral index $\alpha = -2.364$ and a temperature of 3206 K at 60 MHz.[11] The inferred background spectrum from our data is best fitted by a power law of index $\alpha = -2.9$ with a temperature of 2340 K at 60 MHz. If we assume the background spectrum of de Oliveira-Costa et al. (2008) to be true, then our data imply a lunar brightness temperature (thermal emission) of around 1000 K with a lunar albedo at 7 per cent, or a lunar albedo of around 30 per cent with a lunar brightness temperature to 230 K. The nominal values for the lunar albedo (7 per cent) and thermal emission (230 K blackbody) have been taken from measurements at higher frequencies ($\nu > 200$ MHz). The lowest frequency measurements of the lunar thermal emission that we are aware of is the one at 178 MHz by Baldwin (1961), where the authors did not find significant deviation from the nominal value of 230 K. The penetration depth into the lunar regolith for radiation with wavelength λ is $\sim 100\lambda$ (Baldwin 1961). Though significant uncertainties persist for penetration depth estimates, using the above value, the penetration depth in our observation bandwidth varies between 375 and 860 m. Lunar regolith characteristics have not been constrained at these depths so far. Nevertheless, given the high amount (10–20 per cent) of systematics in our estimate of the background temperature spectrum (due to confusion from unmodelled flux in the field), any suggestions of evolution of lunar properties at lower frequencies (larger depths) at this point is highly speculative. In any case, we expect future observations proposed in Section 4.5 to resolve the current discrepancy we observe in the data.

[11] The de Oliveira-Costa et al. (2008) sky model is a composite of data from various surveys, and as such, may suffer uncertainties due to scaling and zero-point offset in these surveys.

4.4 Earthshine estimation

Given the Earth–Moon distance D, and the effective backscattering cross-section of the Moon[12] $\sigma_{\rm m}$, we can convert the estimated values $\widehat{S}_{\rm es}(\nu)$, to the incident earthshine flux as seen by an observer on the Moon, $S_{\rm inc}(\nu)$:

$$S_{\rm inc}(\nu) = \frac{\widehat{S}_{\rm es}(\nu)\ 4\pi D^2}{\sigma_{\rm m}}. \tag{21}$$

Following Evans (1969), and since the Moon is large compared to a wavelength, its scattering cross-section is independent of frequency, and equals its geometric cross-section times the albedo:

$$\sigma_{\rm m} = 0.07\,\pi R_{\rm m}^2. \tag{22}$$

Using equation (22) in equation (21) gives

$$S_{\rm inc}(\nu) = \frac{4}{0.07}\widehat{S}_{\rm es}(\nu)\left(\frac{D}{R_{\rm m}}\right)^2. \tag{23}$$

Using, $D = 384\,000$ km and $R_{\rm m} = 1738$ km, we get

$$S_{\rm inc}(\nu) \approx 2.8 \times 10^6\ \widehat{S}_{\rm es}(\nu)\ \ {\rm Jy}. \tag{24}$$

Furthermore, $S_{\rm inc}$ (in Jy) can be converted to the effective isotropic radiated power (EIRP) by a transmitter on the Earth within our channel width of $\Delta\nu$ Hz according to

$${\rm EIRP}(\nu) = 4\pi\Delta\nu D^2 S_{\rm inc}(\nu)\, 10^{-26}\ \ {\rm W}. \tag{25}$$

Fig. 9 shows the best estimates $\widehat{S}_{\rm es}(\nu)$ (left-hand y-axis), and the corresponding values of earthshine flux as seen from the Moon $S_{\rm inc}(\nu)$ (right-hand y-axis). The corresponding EIRP levels of transmitters on the Earth in a 200 kHz bandwidth are also indicated. As in Fig. 8, we have plotted the mean and standard deviation of earthshine estimates obtained from seven one-hour syntheses.

Estimates of $S_{\rm inc}(\nu)$ in Fig. 9 form critical inputs to proposed Moon-based dark ages and Cosmic Dawn experiments, such as DARE (Burns et al. 2012). Due to the high-risk nature of space mission, we will conservatively assume that such experiments must attain systematic errors in their antenna temperature spectrum of

[12] Also called the radar cross section (RCS) in radar literature.

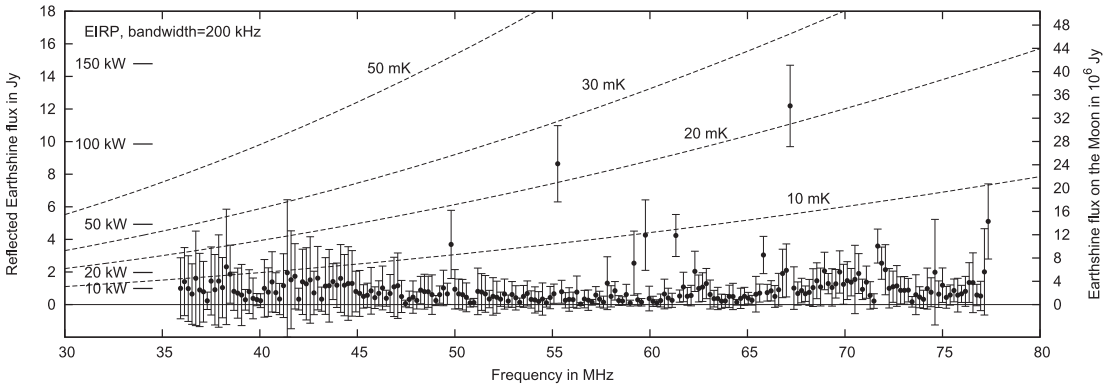

Figure 9. Plot showing the reflected earthshine (left-hand *y*-axis) and earthshine as seen by an observer on the Moon (right-hand *y*-axis). At each frequency channel (195 kHz wide), we measure seven values of earthshine each from a one-hour synthesis images (7 h in total). Plotted are the mean and standard deviation of the seven earthshine values at each frequency channel. Also shown are five EIRP levels of the Earth in a 195 kHz bandwidth. The dotted lines denote the flux level in a single dipole for different brightness temperatures of 10, 20, 30, and 50 mK.

Table 1. Minimum Earth-isolation required for Moon-based dark ages and Cosmic Dawn experiments to achieve an earthshine temperature lower than 1 mK.

Frequency (MHz)	Mean $S_{\rm inc}$(MJy)	Isolation (dB)
35–45	3.6	73
45–55	2	78
55–65	2.7	68
65–75	4.3	69

about 1 mK or lower. Our estimates from Fig. 9 may then be converted to a minimum Earth-isolation that such experiments must design for. We present these estimates for median earthshine values in different frequency bins in Table 1. The values in Fig. 9 may also be renormalized to low-frequency radio astronomy missions to other Solar system locations. For instance, the Earth–Sun Lagrange point L_2 is about 3.9 times further than the Moon, and hence the corresponding values for $S_{\rm inc}$ are about 15 times lower, giving a minimum Earth-isolation that is lower that the values in Table 1 by about 12 dB.

Fig. 9 also shows the Moon-reflected earthshine flux in a single dipole on the Earth corresponding to sky-averaged brightness temperatures of 10, 20, 30, and 50 mK (dashed lines). Since reflected earthshine (from the Moon) is within 20 mK of single-dipole brightness temperature, we expect the presence of the Moon in the sky to not be a limitation to current single-dipole experiments to detect the expected 100-mK absorption feature (Pritchard & Loeb 2010) from Cosmic Dawn with 5σ significance.

Earthshine may also be reflected from man-made satellites in orbit around the Earth. Since single-dipole experiments essentially view the entire sky, the aggregate power scattered from all visible satellites may pose a limitation in such experiments. The strength of reflected earthshine scales as σd^{-4} where d is the distance to the scattering object, and σ is its scattering cross-section. Due to the d^{-4} scaling, we expect most of the scattered earthshine to come from low Earth orbit (LEO) satellites which orbit the Earth at a height of 400–800 km. To proceed with approximate calculations, we will assume that transmitters are uniformly distributed on the Earth, and that their transmission is beamed towards their local horizon. A LEO satellite will then scatter radiation from transmitters situated on a circular rim on the Earth along the tangent points as viewed from the satellite. A simple plane-geometry calculation shows that at a 400 km height, a LEO satellite receives from only 34 per cent of the transmitters as compared to the moon. This ratio increases to about 46 per cent at an 800 km height. Using the above ratios and the σd^4 scaling, we conclude that the scattering cross-section of a satellite that scatters the same power into a single dipole as the Moon (1–2 Jy) to be about 2.4 m^2 at 400 km height and 27 m^2 at 800 km height. We expect the majority of the scattered power to come from large satellites and spent rocket stages as their sizes are comparable to or larger than a wavelength. The myriad smaller ($<$10 cm) space debris, though numerous, are in the Rayleigh scattering limit and may be safely ignored.[13] Moreover, the differential delay in backscattering from different satellites is expected to be sufficient to decorrelate RFI of even small bandwidths of 10 kHz. Hence, we can add the scattering cross-sections of all the satellites to calculate an effective cross-section. Assuming a 10-Jy backscatter power limit for reliable detection of the cosmic signal with a single dipole,[14] we conclude that the effective cross-section of satellites (at 800 km), should be lower than 175 m^2. For a height of 400 km, we arrive at a cross-section bound of just 15 m^2.[15] Since there are thousands of catalogued satellites and spent rocket stages in Earth orbit,[16] reflection from man-made objects in Earth-orbit may pose a limitation to Earth-based Cosmic Dawn experiments.

4.5 Next steps

Due to the pilot nature of this project, we chose to observe the Moon when it was in a field that presented a high brightness contrast (close to the Galactic plane) facilitating an easy detection, and when the Moon reached its highest elevation in the sky as viewed by LOFAR. The latter choice put the Moon close to the bright source 3C144, and may have contributed to a large systematic error in the background temperature spectrum measurements (see Fig. 8). In future observations we plan to mitigate this systematic using two complementary

[13] This is because in the Rayleigh scattering limit, the cross-section of an object of dimension x scales as x^6.

[14] This corresponding to 20 mK of antenna (single dipole) temperature at 65 MHz – required for a 5σ detection of the Cosmic Dawn absorption feature.

[15] These values may not be interpreted as *backscattering* cross-section, but rather as an effective cross-section that is dependent on the transmitter–satellite–telescope geometry.

[16] See fig. II from UN office for Outer Space Affairs (1999).

approaches: (i) choice of a better field (in the Galactic halo) for easier bright source subtraction, and (ii) exploiting the 12 deg d^{-1} motion of the Moon to cancel weaker sources through internight differencing (Shaver et al. 1999; McKinley et al. 2013). In practice, residual confusion may persist due to differential ionospheric and primary-beam modulation between the two nights. Our next steps involve evaluating such residual effects.

We will now assume perfect cancellation of sidelobe noise and compute the thermal uncertainty one may expect in such an experiment. Since the SEFD is lower towards the Galactic halo, we use the value of 28 kJy (van Haarlem et al. 2013) rather than the ones derived in Section 4.1. Conservatively accounting for a sensitivity loss factor of 1.36 due to the time variable station projection in a 7 h synthesis, we expect an effective SEFD of about 38 kJy. Taking into account the fact that the LOFAR baselines resolve the Moon to different extents, we compute a thermal uncertainty in Moon-background temperature contrast measurement (via internight differencing) in a 1 MHz bandwidth of 5.7 K. The poorer sensitivity of the occultation based technique as compared to a single-dipole experiment with the same exposure time ensues from LOFAR's low snapshot filling factor for baselines that are sensitive to the occultation signal ($<100\lambda$). In contrast, the Square Kilometre Array Phase-1 (SKA1) will have a low-frequency aperture array (50–350 MHz) with a filling factor of 90 per cent in its 450 m core.[17] Lunar occultation observations with SKA1-Low can thus yield a significant detection of the 21 cm signal from Cosmic Dawn in a reasonable exposure time (several hours).

In the near-term with LOFAR, a background spectrum with an uncertainty of few kelvin, will place competitive constraints on Galactic synchrotron emission spectrum at very low frequencies (<80 MHz). Additionally, since the thermal emission from the Moon at wavelength λ comes primarily from a depth of $\sim 100\lambda$ (Baldwin 1961), such accuracies may also provide unprecedented insight into lunar regolith characteristics (albedo and temperature evolution) up to a depth of $\sim$1 km.

5 CONCLUSIONS AND FUTURE WORK

In this paper, we have presented a theoretical framework for estimating the spectrum of the diffuse radio sky (or the global signal) interferometrically using lunar occultation. Using LOFAR data, we have also demonstrated this technique observationally for the first time. Further refinement of this novel technique may open a new and exciting observational channel for measuring the global redshifted 21 cm signal from the Cosmic Dawn and the Epoch of Reionization. We find the following:

(i) We observationally confirm predictions that the Moon appears as a source with negative flux density (-25 Jy at 60 MHz) in interferometric images between 35 and 80 MHz (see Fig. 5) since its apparent brightness is lower than that of the background sky that it occults. Consequently, we find the apparent brightness temperature of the Moon to be sufficiently (up to 10–20 per cent systematic measurement error on its flux) described by (a) its intrinsic 230-K blackbody emission as seen at higher frequencies (Heiles & Drake 1963; Krotikov & Troitskii 1963), (b) reflected Galactic emission (Moon position dependent) which is about 160 K at 60 MHz with a spectral index of -2.24, and (c) reflected earthshine comprising of the reflected RFI from the Earth. Lack of reliable estimates of earthshine was the limiting factor in prior work done by McKinley et al. (2013).

(ii) Lunar images in some frequency channels have a compact positive flux source at the centre of the (negative flux) lunar disc. We attribute this compact source to be due to reflected earthshine (RFI), and observationally confirm predictions that the earthshine reflection off the lunar regolith is mostly specular in nature. We demonstrated how this earthshine can be independently measured using resolution afforded by LOFAR's long ($>100\lambda$) baselines. Consequently, reflected earthshine is currently not a limiting factor for our technique.

(iii) Our earthshine measurements between 35 and 80 MHz imply an Earth flux as seen from the Moon of 2–4 $\times$ 10^6 Jy (frequency dependent), although this value may be as high as 35 $\times$ 10^6 Jy in some isolated frequency channels. These values require Dark Ages and Cosmic Dawn experiments from a lunar platform to design for a nominal earthshine isolation of better than 80 dB to achieve their science goals (assuming a conservative upper bound for RFI temperature in a single dipole of 1 mK).

(iv) For Earth-based Cosmic Dawn experiments, reflected RFI from the Moon results in an antenna temperature (single dipole) of less than 20 mK in the frequency range 35 to 80 MHz, reaching up to 30 mK in isolated frequency channels. This does not pose a limitation for a significant detection of the 100 mK absorption feature expected at 65 MHz ($z = 20$). However, if the effective cross-section of visible large man-made objects (satellite and rocket stages) exceeds 175 m^2 at 800 km height, or just 15 m^2 at 400 km height, then their aggregate reflected RFI will result in a single-dipole temperature in excess of 20 mK – a potential limitation for Earth-based single-dipole Cosmic Dawn experiments.

(v) We plan to mitigate the current systematic limitations in our technique through (a) lunar observations in a suitable field away from complex and bright Galactic plane, and (b) interday differencing of visibilities to cancel confusion from the field while retaining the lunar flux (the Moon moves by about 12 deg d^{-1}). We expect to reach an uncertainty of $\sim$10 K in our reconstruction of the radio background. If successful, such a measurement may not only constrain Galactic synchrotron models, but also place unprecedented constraints on lunar regolith characteristics up to a depth of $\sim$1 km.

[17] Based in the SKA1 system baseline design document: https://www.skatelescope.org/home/technicaldatainfo/key-documents/.

ACKNOWLEDGEMENTS

We thank Professor Frank Briggs for bringing to our notice an unnecessary approximation to equation (7) made in an earlier version of the manuscript. We thank the computer group at the Kapteyn Institute for providing the PYTHON modules that we used to render Fig. 4. HKV and LVEK acknowledge the financial support from the European Research Council under ERC-Starting Grant FIRSTLIGHT - 258942. CF acknowledges financial support by the *Agence Nationale de la Recherche* through grant ANR-09-JCJC-0001-01. LOFAR, the Low Frequency Array designed and constructed by ASTRON, has facilities in several countries, that are owned by various parties (each with their own funding sources), and that are collectively operated by the International LOFAR Telescope (ILT) foundation under a joint scientific policy.

REFERENCES

Baldwin J. E., 1961, MNRAS, 122, 513
Bennett A. S., 1962, Mem. R. Astron. Soc., 68, 163
Burns J. O. et al., 2012, Adv. Space Res., 49, 433
Chippendale A. P., 2009, PhD thesis, Univ. Sydney

Daniels F. B., 1963, J. Geophys. Res., 68, 449
de Oliveira-Costa A., Tegmark M., Gaensler B. M., Jonas J., Landecker T. L., Reich P., 2008, MNRAS, 388, 247
Erickson W. C., Kundu M. R., Mahoney M. J., Gergely T. E., 1977, Sol. Phys., 54, 57
Evans J. V., 1969, ARA&A, 7, 201
Furlanetto S. R., Oh S. P., Briggs F. H., 2006, Phys. Rep., 433, 181
Górski K. M., Hivon E., Banday A. J., Wandelt B. D., Hansen F. K., Reinecke M., Bartelmann M., 2005, ApJ, 622, 759
Grobler T. L., Nunhokee C. D., Smirnov O. M., van Zyl A. J., de Bruyn A. G., 2014, MNRAS, 439, 4030
Harker G. J. A., Pritchard J. R., Burns J. O., Bowman J. D., 2012, MNRAS, 419, 1070
Harrington R. F., 2001, Time-harmonic Electromagnetic Fields. Wiley, New York
Heiles C. E., Drake F. D., 1963, Icarus, 2, 281
Kazemi S., Yatawatta S., 2013, MNRAS, 435, 597
Kazemi S., Yatawatta S., Zaroubi S., Lampropoulos P., de Bruyn A. G., Koopmans L. V. E., Noordam J., 2011, MNRAS, 414, 1656
Krotikov V. D., Troitskii V. S., 1963, SvA, 6, 845
McKinley B. et al., 2013, AJ, 145, 23
Mirocha J., Harker G. J. A., Burns J. O., 2013, ApJ, 777, 118
Moffat P. H., 1972, MNRAS, 160, 139
Offringa A. R. et al., 2013, A&A, 549, A11
Patra N., Subrahmanyan R., Raghunathan A., Udaya Shankar N., 2013, Exp. Astron., 36, 319
Perley R., Butler B., 2015, AAS Meeting #225, An Accurate Flux Density Scale from 50 MHz to 50 GHz. Am. Astron. Soc., p. 311.06
Pritchard J. R., Loeb A., 2010, Phys. Rev. D, 82, 023006
Rogers A. E. E., Bowman J. D., 2012, Radio Sci., 47, 0
Shaver P. A., Windhorst R. A., Madau P., de Bruyn A. G., 1999, A&A, 345, 380
Thompson A. R., Moran J. M., Swenson G. W., 2007, Interferometry and Synthesis in Radio Astronomy. Wiley, New York
UN office for Outer Space Affairs, 1999, Technical Report on Space Debris. United Nations, New York
van Haarlem M. P. et al., 2013, A&A, 556, A2
Vedantham H. K., Koopmans L. V. E., 2014, MNRAS, preprint (arxiv:1412.1420)
Voytek T. C., Natarajan A., Jáuregui García J. M., Peterson J. B., López-Cruz O., 2014, ApJ, 782, L9

APPENDIX A: INTERFEROMETRIC RESPONSE TO A GLOBAL SIGNAL

This section provides the intermediate steps in the derivation of equation (2) from equation (1). Equation (1) is

$$V(\bar{u},\nu) = \frac{1}{4\pi}\int \mathrm{d}\Omega\; T_{\rm sky}(\bar{r},\nu)\mathrm{e}^{-2\pi \mathrm{i}\bar{u}.\bar{r}}. \tag{A1}$$

The exponential in the integrand can be cast in a spherical harmonic expansion as[18] (Harrington 2001)

$$\mathrm{e}^{-2\pi \mathrm{i}\bar{u}.\bar{r}} = 4\pi\sum_{l=0}^{\infty}\sum_{m=-l}^{l}\mathrm{i}^l\mathcal{J}_l(2\pi|\bar{u}||\bar{r}|)Y_{lm}(\theta_r,\phi_r)Y^{\star}_{lm}(\theta_u,\phi_u) \tag{A2}$$

where $\mathcal{J}_l$ is the spherical Bessel function of the first kind of order l, Y_{lm} are the spherical harmonics for mode (l, m), $(|\bar{r}|,\theta_r,\phi_r)$ are the spherical coordinates of the direction vector $\bar{r}$, and $(|\bar{u}|,\theta_u,\phi_u)$ are the spherical coordinates of the baseline vector $\bar{u}$.

[18] Also called plane wave expansion, or Rayleigh's expansion after Lord Rayleigh.

Using, $|\bar{r}| = 1$, substituting equation (A2) in equation (A1), and interchanging the order of integration and summation, we get

$$V(\bar{u},\nu) = \sum_{l=0}^{\infty}\sum_{m=-l}^{l}\mathrm{i}^l\mathcal{J}_l(2\pi|\bar{u}|)Y_{lm}(\theta_u,\phi_u) \times \int \mathrm{d}\Omega T_{\rm sky}(\bar{r},\nu)Y^{\star}_{lm}(\theta_r,\phi_r). \tag{A3}$$

The above integral is simply the spherical harmonic expansion of the sky brightness distribution: $T^{lm}_{\rm sky}(\nu)$. This gives us

$$V(\bar{u},\nu) = \sum_{l=0}^{\infty}\sum_{m=-l}^{l}\mathrm{i}^l\mathcal{J}_l(2\pi|\bar{u}|)Y_{lm}(\theta_u,\phi_u)\,T^{lm}_{\rm sky}(\nu). \tag{A4}$$

Equation (A4) shows that the measured visibility on a given baseline is simply a weighted sum of the spherical harmonic coefficients of the sky brightness temperature distribution. The weights are a product of the baseline length dependent factor $\mathcal{J}_l(2\pi|\bar{u}|)$ and a baseline orientation dependent factor $Y_{lm}(\theta_u,\phi_u)$.

If the sky is uniformly bright (global signal only), then

$$T^{lm}_{\rm sky}(\nu) = \left\{\begin{array}{ll} T_{\rm B}(\nu) & l=m=0 \\ 0 & \text{otherwise}\end{array}\right\}. \tag{A5}$$

Substituting this in equation (A4), we get

$$V(\bar{u}) = T_{\rm B}\,\mathcal{J}_0(2\pi|\bar{u}|) = T_{\rm B}\,\frac{\sin(2\pi|\bar{u}|)}{2\pi|\bar{u}|}, \tag{A6}$$

which is equation (2).

APPENDIX B: REFLECTED EMISSION

We compute the intensity of Galactic and extragalactic emission reflected from the Moon using ray tracing with an assumption of specular reflection. Under this assumption, given the Earth–Moon geometry, every pixel on the lunar surface corresponds to a unique direction in the sky that is imaged on to the lunar pixel as seen by the telescope. The algorithm used in computation of reflected emission at each epoch is summarized below.

(i) Define a HEALPIX (Górski et al. 2005) grid ($N = 32$) on the lunar surface. Given RA, Dec. of the Moon and UTC extract all the pixels 'visible' from the telescope location. Compute the position vector $\hat{i}$, and surface normal vector $\hat{n}$ for each pixel.

(ii) For each lunar pixel $\hat{i}$, define the plane of incidence and reflection using two vectors: (a) normal $\hat{n}$, and (b) vector $\hat{t} = (\hat{n}\times\hat{r_p})\times\hat{n}$ tangential to the surface.

(iii) For each lunar pixel $\hat{i}$, the corresponding direction vector which images on to that pixel is then given by $\hat{r} = (\hat{i}.\hat{t})\hat{t} + (-\hat{i}.\hat{n})\hat{n}$.

(iv) Re-grid the sky model from de Oliveira-Costa et al. (2008) on the grid points specified by vectors $\hat{r}$. We use gridding by convolution with a Gaussian kernel since a moderate loss of resolution is not detrimental to our computations. The value of each pixel in the re-gridded map $t^{\hat{i}}_{\rm I}(\nu)$ gives the temperature of incident radiation from direction $\hat{r}$ on the corresponding pixel $\hat{i}$ on the Moon at frequency ν. The subscript I denotes that this is the incident intensity.

(v) The temperature of reflected emission from each pixel $\hat{i}$ is then given by

$$t^{\hat{i}}_{\rm R} = \underbrace{0.07}_{\text{albedo}}\;\underbrace{\hat{n}.\hat{i}}_{\text{projection}}\;t^{\hat{i}}_{\rm I}, \tag{B1}$$

where subscript R denotes that this is the reflected intensity.

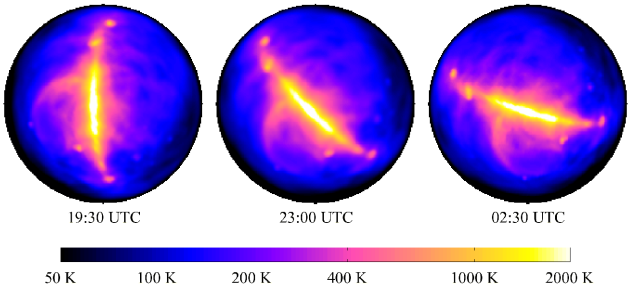

Figure B1. Images showing the apparent brightness temperature of the lunar surface at $\nu = 60$ MHz due to reflected Galactic and extragalactic emission assuming specular reflection with a polarization independent albedo of 7 per cent. The three panels correspond to three epochs at the beginning, middle, and end of the synthesis, the data for which are presented in this paper.

(vi) Cast the Moon pixel coordinates in an appropriate map-projection grid. We use the orthographic projection (projection of a sphere on a tangent plane).

Fig. B1 shows images of the computed apparent temperature of the lunar surface at $\nu = 60$ MHz due to reflection of Galactic and extragalactic emission. We only show images for three epochs: beginning, middle, and end of our synthesis for which we presented data in this paper. The disc-averaged temperature in the images is $\approx$160 K (at 60 MHz). Most of the apparent temporal variability (rotation) in the images is primarily due to the change in parallactic angle. The time variability of the disc-averaged temperature is $\sim$1 K, and is discounted in subsequent analysis.

APPENDIX C: ANGULAR SIZE OF REFLECTED EARTHSHINE

As shown in Fig. C1, we compute the angular size of reflected earthshine $\Delta\theta_{es}$ by tracing the critical ray that emanates from the tangent point on the Earth (B), undergoes specular reflection on the lunar surface at A, and enters the telescope at T. The angle of incidence and reflection are then given by

$$i = r = \phi + \frac{\Delta\theta_{es}}{2}. \tag{C1}$$

Using $\sin(x) \approx x$ for $x \ll 1$ and applying the sine rule in triangle AMT, we get

$$\frac{\phi}{D - R_m - R_e} \approx \frac{\Delta\theta_{es}/2}{R_m}, \tag{C2}$$

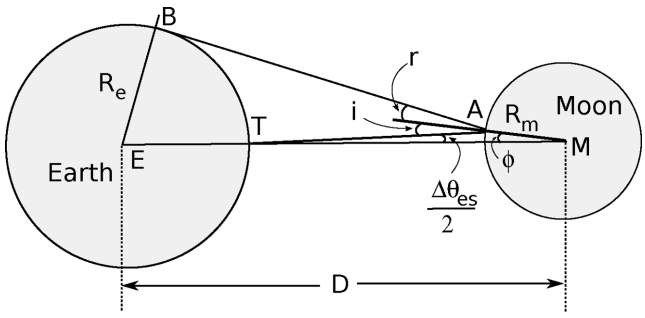

Figure C1. Not-to-scale schematic of the Earth–Moon geometry used in the calculation of the angular size of reflected earthshine.

where we have approximated the length of segment AT by $D - R_m - R_e$. Similarly, sine rule in triangle ABE gives

$$\frac{i + r}{R_e} = \frac{2i}{R_e} = \frac{\sin(\frac{\pi}{2})}{D - R_m}. \tag{C3}$$

Eliminating i and ϕ between equations (C1), (C2), and (C3) we get

$$\Delta\theta_{es} = \frac{R_m R_e}{(D - R_m)(D - R_e)}, \tag{C4}$$

which under the assumptions $D \gg R_m$ and $D \gg R_e$ yields

$$\Delta\theta_{es} \approx \frac{R_m R_e}{D^2}, \tag{C5}$$

which is equation (12). For typical values for the Earth–Moon geometry, we get $\Delta\theta_{es} \approx 16$ arcsec.

We have so far assumed that the reflection is perfectly specular. We will now relax this assumption, and compute the 'angular broadening' of the reflected image of a transmitter at T. We will use the notation in Fig. C1. Let $\theta/2$ be the angle ATM, and ϕ as before be the angle AMT. Let the distance AT be x. If the lunar terrain in the vicinity of point A, presents a slope of ϕ, then a ray travelling along TA will be reflected back to T. To understand the angular broadening of the backscatter, we need to compute the relationship between θ and ϕ. Cosine rule in triangle AMT gives

$$x^2 = (D - R_e)^2 + R_m^2 - 2(D - R_e)(R_m). \tag{C6}$$

Combining this with the sine rule in triangle AMT, we get

$$\sin(\theta/2) = \frac{R_m \sin\phi}{\sqrt{(D - R_e)^2 + R_m^2 - 2(D - R_e)R_m \cos\phi}}. \tag{C7}$$

Using the small angle approximation, and $D - R_e \gg R_m$, we get

$$\theta \approx 2\frac{R_m}{D - R_e}\phi. \tag{C8}$$

For the Earth–Moon geometry, we get $\theta \approx 9.2 \times 10^{-3}\phi$. Radar backscatter data has shown that the rms slope on the lunar surface is about 14 deg (Daniels 1963). This implies an rms width of the broadened image to be $\theta \approx 3.86$ arcmin.

[1]*Kapteyn Astronomical Institute, PO Box 800, NL-9700 AV Groningen, the Netherlands*
[2]*Netherlands Institute for Radio Astronomy (ASTRON), Postbus 2, NL-7990 AA Dwingeloo, the Netherlands*
[3]*Department of Physics and Astronomy, University College London, Gower Street, London WC1E 6BT, UK*
[4]*SKA South Africa, 3rd Floor, The Park, Park Road, Pinelands 7405, South Africa*
[5]*Department of Physics and Elelctronics, Rhodes University, PO Box 94, Grahamstown 6140, South Africa*
[6]*Harvard–Smithsonian Center for Astrophysics, 60 Garden Street, Cambridge, MA 02138, USA*
[7]*Max Planck Institute for Astrophysics, Karl Schwarzschild Str. 1, D-85741 Garching, Germany*
[8]*Department of Astronomy and Oskar Klein Centre, Stockholm University, AlbaNova, SE-10691 Stockholm, Sweden*
[9]*Research School of Astronomy and Astrophysics, Australian National University, Mt Stromlo Obs., via Cotter Road, Weston, ACT 2611, Australia*
[10]*Helmholtz-Zentrum Potsdam, DeutschesGeoForschungsZentrum GFZ, Department 1: Geodesy and Remote Sensing, Telegrafenberg, A17, D-14473 Potsdam, Germany*
[11]*Leibniz-Institut für Astrophysik Potsdam (AIP), An der Sternwarte 16, D-14482 Potsdam, Germany*
[12]*Shell Technology Center, Bangalore 560 048, India*
[13]*CSIRO Australia Telescope National Facility, PO Box 76, Epping, NSW 1710, Australia*

[14]*University of Twente, NL-7522 NB Enschede, the Netherlands*
[15]*Institute for Astronomy, University of Edinburgh, Royal Observatory of Edinburgh, Blackford Hill, Edinburgh EH9 3HJ, UK*
[16]*University of Hamburg, Gojenbergsweg 112, D-21029 Hamburg, Germany*
[17]*School of Physics and Astronomy, University of Southampton, Southampton SO17 1BJ, UK*
[18]*Department of Astrophysics/IMAPP, Radboud University Nijmegen, PO Box 9010, NL-6500 GL Nijmegen, the Netherlands*
[19]*SmarterVision BV, Oostersingel 5, NL-9401 JX Assen, the Netherlands*
[20]*Thüringer Landessternwarte, Sternwarte 5, D-07778 Tautenburg, Germany*
[21]*Hamburger Sternwarte, Gojenbergsweg 112, D-21029 Hamburg, Germany*
[22]*Astrophysics, University of Oxford, Denys Wilkinson Building, Keble Road, Oxford OX1 3RH, UK*
[23]*Laboratoire Lagrange, UMR7293, Universitè de Nice Sophia-Antipolis, CNRS, Observatoire de la Cóte d'Azur, F-06300 Nice, France*
[24]*Leiden Observatory, Leiden University, PO Box 9513, NL-2300 RA Leiden, the Netherlands*
[25]*LPC2E/CNRS, 3A, Avenue de la Recherche Scientifique, F-45071 Orléans cedex 2, France*
[26]*Station de Radioastronomie de Nancay, Observatoire de Paris - CNRS/INSU, USR 704 - Univ. Orleans, OSUC, route de Souesmes, F-18330 Nancay, France*
[27]*Astronomisches Institut der Ruhr-Universität Bochum, Universitaetsstrasse 150, D-44780 Bochum, Germany*
[28]*Astro Space Center of the Lebedev Physical Institute, Profsoyuznaya str. 84/32, Moscow 117997, Russia*
[29]*Max-Planck-Institut für Radioastronomie, Auf dem Hügel 69, D-53121 Bonn, Germany*
[30]*Anton Pannekoek Institute, University of Amsterdam, Postbus 94249, NL-1090 GE Amsterdam, the Netherlands*
[31]*Sodankylä Geophysical Observatory, University of Oulu, Tähteläntie 62, 99600 Sodankylä, Finland*
[32]*STFC Rutherford Appleton Laboratory, Harwell Science and Innovation Campus, Didcot OX11 0QX, UK*
[33]*Centre de Recherche Astrophysique de Lyon, Observatoire de Lyon, 9 av Charles André, F-69561 Saint Genis Laval Cedex, France*
[34]*Fakultät fr Physik, Universität Bielefeld, Postfach 100131, D-33501 Bielefeld, Germany*
[35]*Jodrell Bank Center for Astrophysics, School of Physics and Astronomy, The University of Manchester, Manchester M13 9PL, UK*
[36]*LESIA, UMR CNRS 8109, Observatoire de Paris, F-92195 Meudon, France*

This paper has been typeset from a TEX/LATEX file prepared by the author.